Available online at www.sciencedirect.com
SCIENCE DIRECT
Earth and Planetary Science Letters 239 (2005) 352–367
EPSL
www.elsevier.com/locate/epsl

Numerical modelling of quaternary deformation and post-rifting displacement in the Asal–Ghoubbet rift (Djibouti, Africa)

Rodolphe Cattin [a,*], Cécile Doubre [b,c], Jean-Bernard de Chabalier [d], Geoffrey King [b], Christophe Vigny [a], Jean-Philippe Avouac [a,e], Jean-Claude Ruegg [d]

[a] *Laboratoire de Géologie, Ecole Normale Supérieure, 24 rue Lhomond, 75231, Paris Cedex 05, France*
[b] *Laboratoire de Tectonique - Mécanique de la lithosphère, Institut de Physique du Globe de Paris, Boite 89 - 4 place Jussieu, 75252, Paris cedex 05, France*
[c] *Department of Earth and Space Sciences, University of California, Los Angeles, 595 Charles Young Drive East, Box 95156, Los Angeles, CA 90095-156, USA*
[d] *Laboratoire de Sismologie - Mécanique de la lithosphère, Institut de Physique du Globe de Paris, Boite 89 - 4 place Jussieu, 75252, Paris cedex 05, France*
[e] *Tectonics Observatory, California Institute of technology, M C 100-23 Pasadena, CA 91125, USA*

Received 2 November 2004; received in revised form 24 May 2005; accepted 25 July 2005
Available online 6 October 2005
Editor: V. Courtillot

Abstract

Over the last three decades a host of information on rifting process relating to the geological and thermal structure, long-time scale deformation (Quaternary and Holocene) and rifting cycle displacement across the Asal–Ghoubbet rift has been made available. These data are interpreted with a two-dimensional thermo-mechanical model that incorporates rheological layering of the lithosphere, dyke inflation and faulting. Active fault locations and geometry are mainly controlled by both thermal structure and magma intrusion into the crust. The distributed slip throughout the inner rift is related to the closeness of magma chamber, leading to additional stress into the upper thinned crust. Assuming a constant Arabia–Somalia motion of 11 mm/year, the variation of subsidence rate between the last 100 and 9 ka is associated with a decrease of the average injection rate from 10 to 5 mm/year. These values, about equal to the regional opening rate, suggest that both volcanism and tectonic play an equivalent role in the rifting process. Our modelled sequence of events gives one possible explanation for both vertical and horizontal displacements observed since the 1978 seismovolcanic crisis. Although part of the post-rifting deformation could be due to viscous relaxation, the high opening rate in the first years after the event and the abrupt velocity change in 1984–1986 argue for a large dyke inflation of 12 cm/year ending in 1985. The asymmetric and constant pattern of the GPS velocity since 1991 suggests that present post-rifting deformation is mainly controlled by fault creep and regional stretching. This study demonstrates the internal consistency of the data set, highlights the role of magmatism in the mechanics of crustal stretching and reveals a complex post-rifting process including magma injection, fault creep and regional stretching.

Keywords: Asal–Ghoubbet; rifting cycle; rift zone; fault creep; dyke inflation; magma injection

1. Introduction

Located at the western tip of the Aden ridge, the Asal–Ghoubbet rift in Republic of Djibouti is the first

* Corresponding author. Tel.: +33 1 44 27 50 85.
E-mail address: cattin@geologie.ens.fr (R. Cattin).

0012-821X/$ - see front matter © 2005 Elsevier B.V. All rights reserved.
doi:10.1016/j.epsl.2005.07.028

subaerial section of the ridge propagating into Afar [1–5]. This rift is often considered to be an analogue for a young slow spreading ridge segment. It comprises a narrow trough bounded by normal faults, volcanism and intense micro-seismic activity [6,7]. The last event is the 1978 seismovolcanic crisis. A seismic swarm began in the rift on 6 November 1978 and lasted for 2 months [8]. The major earthquake (mb = 5.3) occurred near the rift axis on 7 November 1978 close to the coast of the Ghoubbet Bay (Fig. 1). Five to seven faults within the inner floor of the rift slipped 0.15 to 0.5 m over lengths of 4–12 km [8,9]. The earthquake was followed between 7 and 14 November by a volcanic eruption that formed a new volcanic cone named Ardukoba in the north-western part of the rift (Fig. 1).

Over the last three decades a host of information on lithospheric deformation in the Asal–Ghoubbet rift has been made available pertaining both to the long term displacement rate (i.e. Holocene and Quaternary) [10–12] and the rifting cycle deformation [8,9,13–16]. These observations are comparable with the deformation following the spreading episode in the Krafla system (north Iceland), which began in 1975 [17–24].

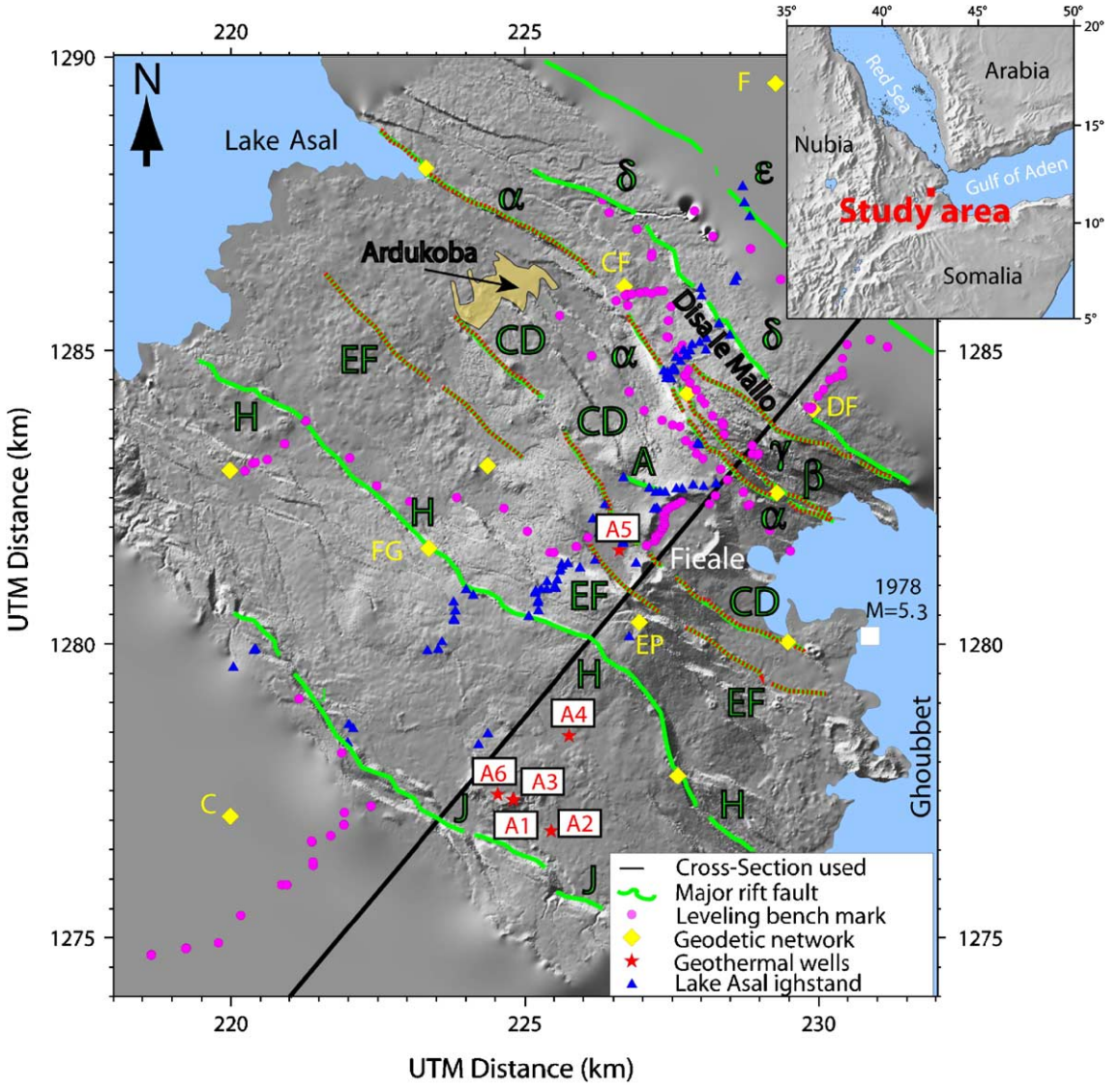

Fig. 1. High resolution Digital Elevation Model of the Asal–Ghoubbet rift showing the 1978 epicenter (white square), the Ardukoba lava, major rift faults (green lines), geothermal wells (red stars) and lake Asal highstand (blue triangles). Red dashed lines show the active fault during the 1978 crisis. Pink circles indicate the levelling benchmarks reported by Ref. [14]. Yellow diamonds show the location of GPS network used in this study. Black line indicates the cross section discussed here after.

Horizontal geodetic measurements and levelling data give very similar results, with the distinction that the deformations cover an area broader at Iceland. The fault geometry in the Asal–Ghoubbet rift is relatively well known from seismic, geodetic and field observations [15,25–27]. The thermal structure at shallow depth (<2 km) is also constrained from geothermal exploration [28,29].

We show that these data can be reconciled on the basis of a single thermo-mechanical model of both long-term and rifting cycle processes. We focus on a N 36° E section across the rift at the longitude of the Fiaele volcano because most of the data pertain to this particular section (Fig. 1). Special emphasis is given either on the localization of long term deformation and on post-rifting deformation since the 1978 crisis because both could be used to constrain thermal structure, rheology and aseismic processes in the Asal–Ghoubbet rift.

After presenting the observations and measurements, we describe the calculated thermal structure and the assumptions on which the numerical modelling approach is based. We compare the long-time scale observations (including faults location, Fiaele topography and lake Asal highstand observations) with model-simulated stress field and surface displacement. We next study the sensitivity of our post-rifting results to dyke location, aseismic slip and time dependence of the dyke opening rate. Finally we propose that transient deformation since the 1978 crisis is controlled by various processes including regional stretching, dyke inflation and aseismic slip.

2. Data sets

2.1. Geometry

In the Ghoubbet Bay and in the Gulf of Tadjurah the seismic activity recorded between 1974 and 1990 reaches 12 km depth [25]. Seismological experiments conducted since 1985 give focal depths (8–15 km) in the Hanlé depression (~30 km south-west from the rift axis) and show a shallow seismicity (<5 km) under the Asal–Ghoubbet rift [25]. A recent seismic experiment including eleven temporary seismometers deployed in addition to the seven permanent stations in the rift confirms a seismogenic crust about 3 km thick below the Fieale volcano. It clearly reveals the asymmetry of the seismic activity where most of the active faults are located in the north-eastern margin of the rift [30]. This is consistent with tectonic and morphological observations which show that the current extensive tectonic activity is concentrated at the north of the rift axis, and especially in the Disa le Mallo subrift [8,27].

The existence of a shallow (2–5 km) magma reservoir with molten material close to the Ardukoba volcano, is suggested by seismic, magnetolleric and gravity studies: In the central part of the inner floor, a large amount of the micro-seismicity recorded since 1979 is concentrated below the Fieale and disappears below a depth between 3 and 5 km [25,30]. Seismic reflection profiles show an anomalous low-velocity mantle under the Asal–Ghoubbet rift [31]. Magnetotelluric data reveals a shallow magma chamber (2–4 km) [32]. The observed gravity increase between 1985 and 1999 is compatible with a 600 m diameter sphere with a positive density contrast of 100 kg/m^3 centered 4 km beneath the surface [33].

The faults' geometry at depth is still unconstrained, particularly those that were inactive during the 1978 seismo-volcanic crisis. However, in the whole sub-aerial rift the hypocentral distribution of micro-seismicity clearly related to major faults shows that seismic slip occurs above 6 km depth [30]. This argues for subvertical fault planes rather than listric faults, in agreement with the study of shear wave splitting [25]. For the activated faults during the 1978 crisis the analysis of co-rifting displacements gives a dip angle between 60° and 80° to a depth of 3 km [15].

2.2. Geothermal field

Since 1970, geothermal exploration in the republic of Djibouti has involved two wells drilled in the Hanlè depression (~30 km south-west from the rift axis) and six other wells in the Asal–Ghoubbet rift [28,29] (Fig 1). These reach depths of 1500–2000 m (Fig. 2) and constrain the temperature field of the shallow crust. In the Hanlé plain temperature measurements give a maximum of 124 °C at 2020 m and a temperature gradient between 1.8 and 2.4 °C/100 m. This low gradient suggests that the crust far from the rift axis is thick without any shallow thermal sources related to intrusions. The wells A1–A2–A3–A6, close to the south-western margin of the rift, all give a maximum temperature of 274 °C at 1600 m and a high gradient ranging from 14 to 20 °C/100 m. The thermal wells A4 and A5 are similar to a depth of 500 m. The temperature of A5 between 500 and 1000 m depth is reduced possibly due to water circulation between Ghoubbet and Lake Asal as inferred from geochemistry [34] and self-potential and Telluric–Telluric prospecting [35].

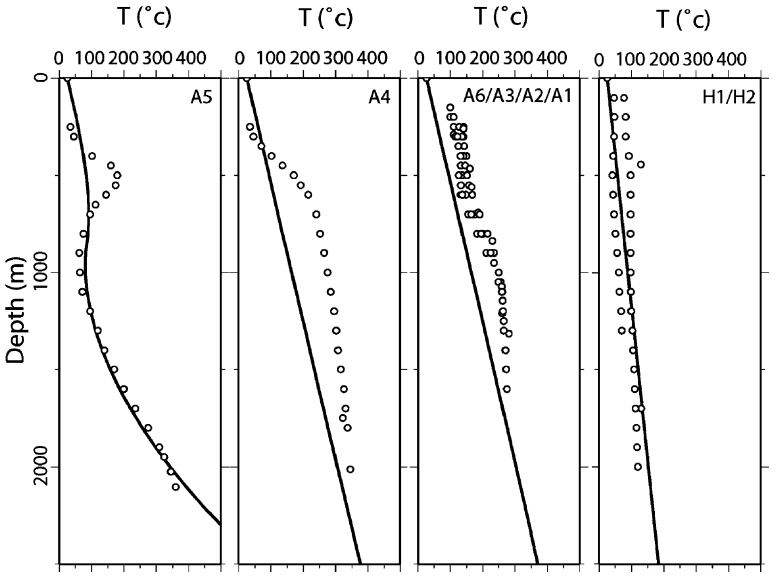

Fig. 2. Calculated (black line) and measured (circles) temperature in depth. The distance to rift axis increases from left (A5) to right (H1/H2). The geothermal wells in the Asal–Ghoubbet rift are labelled with A. The wells H1 and H2 are located in the Hanlè depression 35–40 km SW of the rift axis.

2.3. Deformation across the rift

The deformation across the Asal–Ghoubbet rift was estimated from various approaches that cover different time spans including Quaternary deformation, Holocene vertical motion, and rifting cycle displacement.

The major volcanic edifice of the rift is the Fieale volcano, which has been active from about 300 to 100 ka ago. The Fieale's topography has thus recorded tectonic deformation during the last 100 ka [10]. The spreading rate estimated from the restored topography of the Fieale is 17–29 mm/year with a mean N 40° E direction. The vertical offsets on the major faults give 1–3.5 mm/year of subsidence at Fieale crater relative to the rift 2.5 km away of the rift axis (Fig. 3a). The comparison between extension and subsidence across the rift over that period requires that over 90% of crustal thinning has been compensated by magmatism in the form of dyke intrusion or underplating [10].

Well-preserved lake shorelines indicate a lake level 160 m above sea level during Holocene. Measurements of the age [11] and elevation [12] of the Holocene Highstand of the lake Asal yield a maximum subsidence rate of about 8 mm/year of the rift axis relative to rift shoulders over the last 9 ka (Fig. 3b). The difference between this velocity and the vertical velocities estimated from the deformation of the Fieale volcano suggests that the long term deformation has not been steady state. This is similar to that observed in the Krafla volcanic system (north Iceland), where crustal

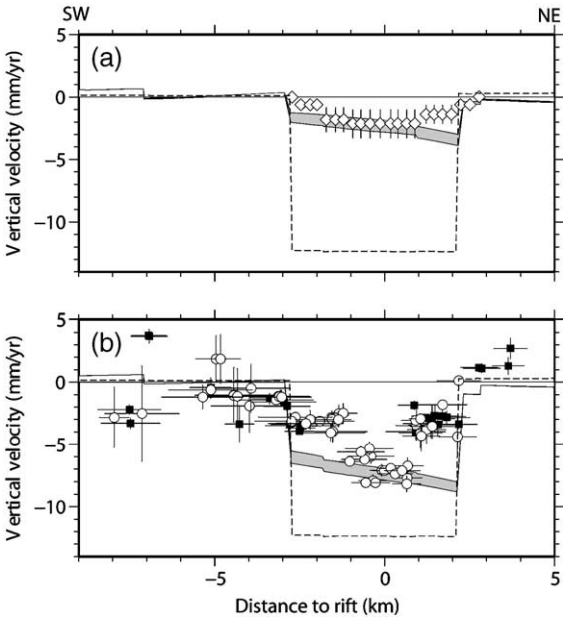

Fig. 3. Calculated and measured long-term vertical velocity projected along the studied profile. Measurements are given with respect to the northernmost highest quality data. Dashed line and grey envelope indicate the calculated velocity with and without injection of magma material, respectively. (a) Vertical velocity estimated by restoring initial topography of the Fieale ~100 ka [8] (circles). The increase of vertical velocity due to additional material ranges from 9.5 to 10.4 mm/year. (b) Holocene velocity from lake Asal highstand observations including radiocarbon date [9] and height measurements [10]. Black and white circles gives the lowest and highest quality observations [9]. The increase of vertical velocity due to additional material is estimated from 4.4 to 5.4 mm/year.

spreading is episodic, with brief episodes of intense activity, separated by long quiescent periods [19]. Assuming a constant regional spreading rate, these changes can be associated with variations in intrusion rate of magma material. This will be discussed in Section 4.

In the Asal–Ghoubbet rift, the most recent crisis is the 1978 seismic sequence followed by extrusion of lava forming Ardukoba volcano, located in the rift axis 8 km northwest of the main shock (Fig. 1). This crisis has been described in detail elsewhere [8,15]. Here, we summarise the co-rifting and post-rifting geodetic measurements (Fig. 3). A levelling line (see location Fig. 1) surveyed in 1972 and 1979 shows about 0.7 m of inner subsidence and about 0.2 m of flank uplift [9,13] (Fig. 4a). Trilateration measurements in 1972/73 and in November 1978 show extension of ~1 m orientated perpendicular to the rift axis (Fig. 4b). The levelling line resurveyed in 1984 and 2000 shows a large and wide uplift (10–15 mm/year) within 10 km of the rift axis (Fig. 4c and e) and a subsidence at the rift axis of 7–15 mm/year relative to the rift margin [14,16]. Fig. 4e shows that these observations are in agreement with vertical velocity estimated from GPS measurements between 1991 and 2003 [16]. These observations are also similar with the 1987–1992 uplift observed in the Krafla system in Iceland due to the 1975 major rifting episode [19–21]. The last levelling data, collected in

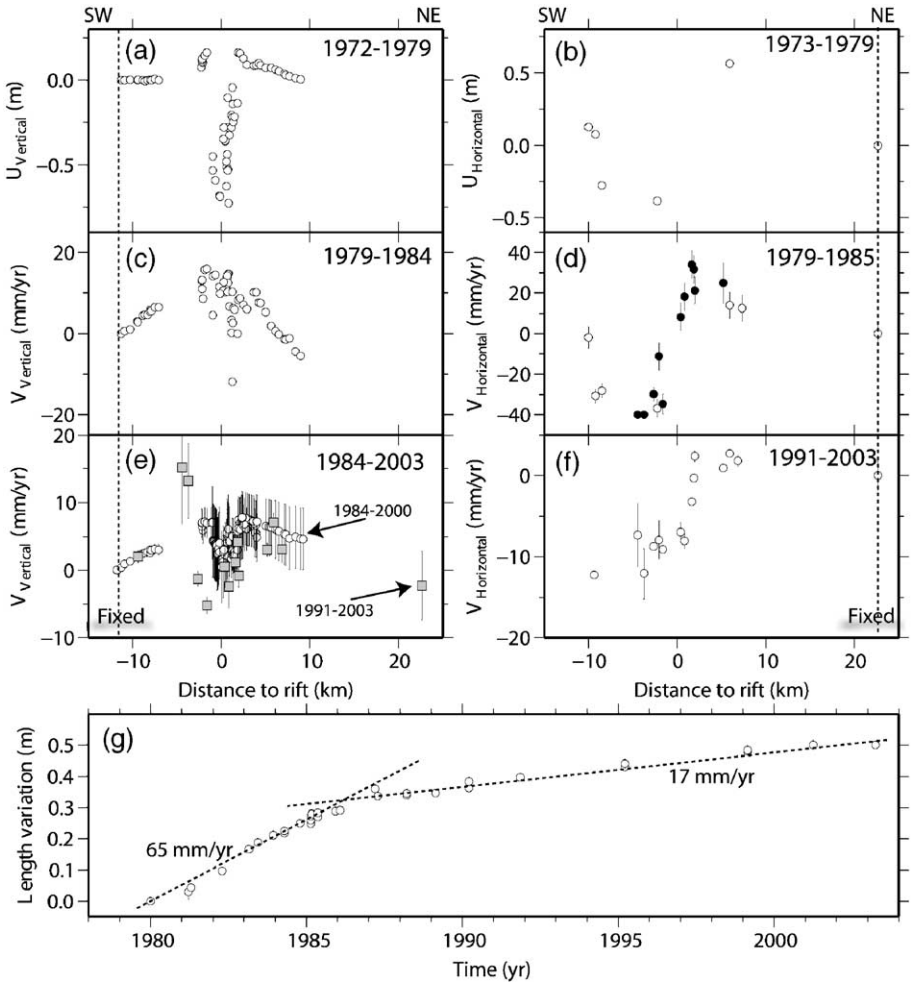

Fig. 4. Geodetic data projected along the section shown in Fig. 1. Vertical and horizontal measurements are given with respect to the southernmost and northernmost data, respectively. The error bars of GPS data show the formal 1-sigma uncertainty. The levelling uncertainty is the cumulative error along the levelling line. (a) Vertical co-rifting displacement from levelling (b) Horizontal co-rifting displacement. (c) Vertical velocity from levelling observations during the 1979–1984 interval. (d) White and black circles give horizontal velocity from trilateration observations between 1979 and 1984, and 1979 and 1985, respectively. (e) Vertical GPS velocity between 1991 and 2003 (grey squares) and levelling measurements from 1984 to 2000 (white circles). (f) Horizontal GPS velocity between 1991 and 2003. (g) Line length variation between 1980 and 2003 between stations EP and DF.

2000 show a trend over the entire profile, with a difference at the end of the line of 7.5 cm [33]. All the levelling lines was measured only in one way (forward run) which does not allow to quantify the instrumental drift. We do not know yet if the data are affected by systematic errors or if this trend reflects a large-scale uplift of the north-eastern part of the rift (see discussion in Ref. [16]). In the following we assume that this trend is real.

The geodetic network (Before 1991: Trilateration—after 1991: GPS) was completed with additional points and resurveyed entirely as in part at least every 2 years between 1979 and 2003. Figs. 4d, f, g and 5 show a decrease of the opening rate of the rift from 65 to 17 mm/year [14,16], with a velocity change in 1984–1986. Thus, the current opening rate is higher than the Arabia–Somalia motion (~11 mm/year) [16]. This observation is similar to the GPS measurements in the Krafla rift showing a spreading rate of 45 mm/year near the rift versus 18 mm/year for the time-averaged spreading rate in north Iceland [21]. As previously proposed [20], these observations confirm that transient compressional deformation may occur in active spreading zone. The possible sources of these transient processes, such as injection of magma material, viscoelastic relaxation or aseismic slip, will be discussed in Section 5.

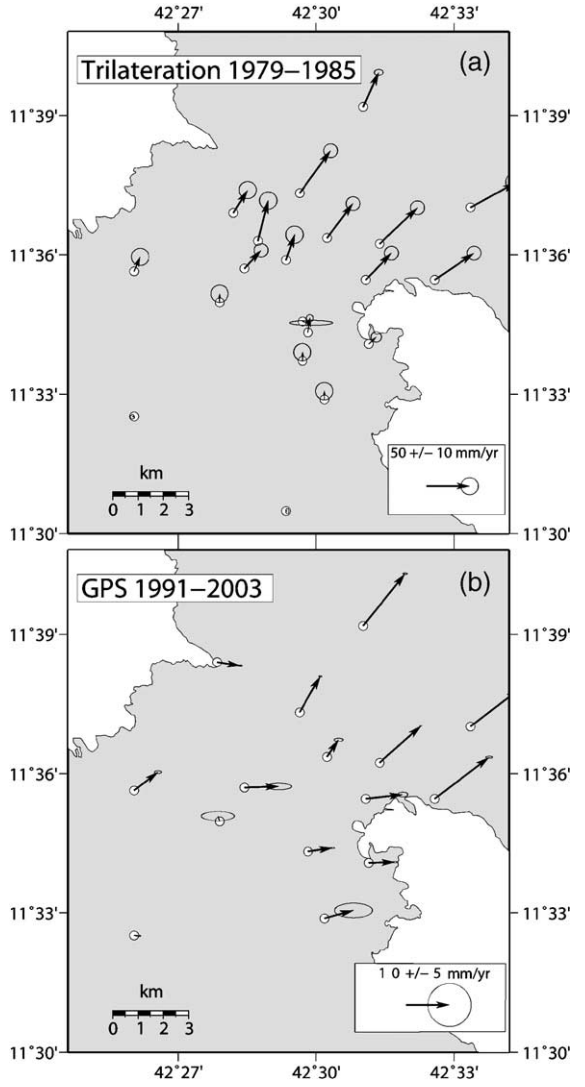

Fig. 5. Post-rifting horizontal velocity relative to Somalian plate: (a) Trilateration measurements between 1979 and 1985 [14]. (b) GPS data between 1991–2003 [16].

3. Modelling approach and assumptions

3.1. Modelling strategy

Our main goal is to quantify the relative role of each post-rifting process including viscous relaxation, dyke inflation and aseismic slip. In our approach these mechanical processes are performed using both the long term deformation (100 ka) and the post-rifting displacement as the initial condition. To enable interaction among these processes and time scales, the following modelling sequence is performed : (1) A spreading rate of 11 mm/year is used as kinematic boundary condition for all the runs. (2) A finite difference formulation is used to model the thermal steady state in a moving symmetric medium. This thermal state is then used as the initial condition for all finite element calculations. (3) To study the localization of the deformation due to this thermal structure the long term (100 ka) deformation is calculated without fault. (4) Next, to obtain the long term state of stress we model magmatic infilling and we introduce the active major faults using a friction coefficient low enough so as to let the faults slip freely. (5) Using this pre-stress lithosphere, we impose the co-rifting slip on the faults EF, CD, α, β and γ and dilatation of the Asal dyke obtained from inversion of geodetic data. (6) The post-rifting phase is next computed by locking the faults and imposing dyke inflation. (7) Finally, faults are selectively unlocked and allowed to creep aseismically. Stages 6 and 7 are performed disjointly with the state of stress obtained at stage 5 (including long term and co-rifting) as initial condition.

This sequence of models has implicit directivity in time that prevents interaction of the later step with the earlier. However the variation of stress within the crust due to rifting cycle is low enough (<20 MPa) in comparison with the long term deviatoric stress (60–150 MPa). Furthermore assuming velocity of magmatic

infilling between 0 to 10 mm/year does not significantly affect (<10%) the temperature field. In the following we thus assume that both temperature field and pre-stress lithosphere represents properly the mean behaviour of the lithosphere over the last 100 ka.

In the next paragraphs we describe in detail the approach for both thermal structure and mechanical modelling.

3.2. Thermal structure

In this paper we compute the thermal structure and deformation field separately because we assume the thermal structure to be in a steady state over 100 ka. Our goal is not to study in detail the physical processes leading to the thermal structure but rather to obtain a temperature field in agreement with geothermal observations, which can be used as the initial condition in the mechanical modelling.

We construct a numerical modelling along a 70 km long N 36° E trending cross section perpendicular to rift axis, from the Hanlé depression located 35 km SW from the rift axis to the southern part of the Danakil Horst near the coast of the Gulf of Tadjura (see Fig. 1 in Ref. [15]). We use a 2-D finite difference scheme of heat conduction in a moving symmetric medium with a grid size of 100 m. The assumed boundary conditions are a constant surface temperature of 25 °C and a depth dependent temperature at the rift axis. We have used a thermal diffusivity of 0.5 mm^2/s and a spreading rate of 11 mm/year derived from recent geodetic data [16]. We have selected the set of parameters that best explains the data of 8 thermal wells in Asal–Ghoubbet rift (A1 to A6) and Hanlè depression (H1 and H2) [28,29]. We have in particular considered a 1.7 km deep negative Gaussian distribution of heat production to simulate the local decrease of temperature due to fluid flow [34,35] near the rift axis. This simple computation yields consistent temperature fields near the Asal rift (A5) as well as in the Hanlé basin (H1–H2) (Fig. 2). The calculated thermal gradients for the A1, A2, A3, A6 thermal wells are also in agreement with measurements. The offset of 50 °C between measured and calculated temperature is due to a high surface heat flow which is not taken into account in our modelling. Local thermal effects associated with water flow within the shallow crust could explain the disagreement between the calculated and measured temperature in the A4 thermal wells. Here we study the thermal structure on a larger scale and the estimation of such shallow local scale is beyond the scope of this paper. The thermal wells give the temperature to a depth of 2 km. In Section 4 we will constrain the thermal structure of the deeper part of the lithosphere by studying the increase of the thickness of the seismogenic layer with the distance to rift axis.

3.3. Rheology

For the thermo-mechanical approach we use a 2-D finite element model, ADELI [36] that accounts for the rifting cycle and the non-Newtonian behaviour of the lithosphere and its dependency on temperature and pressure. A depth-varying rheology has been incorporated with elasto-brittle deformation in the upper part of the lithosphere and ductile deformation in the lower part. The empirical rheological equations and laboratory-derived basalt properties [37–39] are used under the assumption that they can be extrapolated to geological conditions.

Under low stresses and low temperature, rocks deform elastically. For isotropic materials the relationship between each component of strain (ε_{ij}) and stress (σ_{ij}) is written

$$\varepsilon_{ij} = \frac{1+\nu}{E}\sigma_{ij} - \frac{\nu}{E}\sigma_{kk}\delta_{ij} \quad (1)$$

where E and ν are the Young's modulus and the Poisson's ratio, respectively.

Beyond the elastic domain, rocks deform brittley or ductily. We use an elasto-plastic pressure dependent law with the failure criterion of Drucker–Prager [37]. Failure occurs if

$$\frac{1}{2}(\sigma_1 - \sigma_3) = \left[c(\cot\phi) + \frac{1}{2}(\sigma_1 + \sigma_3)\right]\sin\phi \quad (2)$$

where c is the cohesion, ϕ is the internal friction angle.

Ductile flow in the lithosphere is empirically described by a law which relates the critical principal stress difference necessary to maintain a steady-state strain-rate to a power of the strain-rate [37–39]. This power-law creep is written

$$\dot{\varepsilon} = A_p(\sigma_1 - \sigma_3)^n \exp\left(-E_p/RT\right), \quad (3)$$

where R is the universal gas constant, T is the temperature, E_P is the activation energy, and A_P and n are empirically determined material "constants", assumed not to vary with stress and (P,T) conditions. The ductile flow-law is thus strongly dependent on rock type and temperature.

In this paper we use typical material properties for an oceanic lithosphere [40]: E=90 GPa, ν=0.25, c=10 MPa, ϕ=30°, A_P=7.10^{-14} Pa^{-n} s^{-1}, n=3, E_P=510

kJ mol^{-1} and a density $\rho = 2800$ kg m^{-3}. The calculated temperature field described in the previous section is prescribed as an initial condition (see Section 3.1) and does not evolve during the simulation.

The relaxation time associated with the lowest viscosity value ($\eta \sim 5.10^{17}$ Pa s) is ~2 months. For all computation we chose a time step of ~1 month and ~5 h to model long-term and rifting cycle deformation, respectively.

3.4. Geometry and boundary conditions

The main features of our model are presented in Fig. 6. The boundary conditions applied to the system are constrained by geodynamics and GPS data [16]: on both northern and southern vertical face we apply a 5.5 mm/year horizontal rate of extension and we leave vertical velocities free. The model is loaded with gravitational body forces and the structure is supported by hydrostatic pressure at its base to allow isostatic compensation. Only minor erosion and deposition occur in this arid area; thus we neglect surface processes in our approach and the upper surface of the model is free of stresses.

The faults' geometry is constrained from [15,27]. A simple static friction law is assumed along the faults

$$|\sigma_T| - \mu' \sigma_N \leq 0, \quad (4)$$

where μ' is the effective friction coefficient including pore pressure and σ_T and σ_N are the normal and the shear stress on the fault, respectively. We use a dry Coulomb–Navier criterion which underestimates the "real" friction coefficient. Numerically, a fault is simulated by contact between nodes on each side of the discontinuity [41]. Elements are sized $\Delta l \sim 650$ m except within the rift axis where a dense mesh is used over a 8 km band ($\Delta l \sim 200$ m). The main limitation of this modelling is that we do not consider finite length of faults or strike slip due to the two dimensional extent of the study.

4. Long time scale deformation

4.1. Localization of the deformation

In the first stage of modelling, we assume that the Asal–Ghoubbet rift is a homogeneous medium with no active fault initially introduced. The long-term deformation is calculated by stretching the lithosphere for 100 ka with a rate of 11 mm/year and using the calculated temperature field as the initial condition plastic deformation appears after ~5 ka and a steady state velocity field is reached after 10 ka. We consider that numerical steady state is attained when the velocity field does not evolve any more ($\delta V/V < 5\%$). The location of the cross section study is given in Fig. 1. Cumulative plastic strain first appears in the rift axis at 4 km depth and reaches the surface with two newly formed antithetic shear zones. This deformation pattern appears to be mainly controlled by the thermal structure. To test the temperature of the deeper part of the lithosphere we study both the seismogenic layer (Fig. 7a) and the locations of the active faults (Fig. 7b).

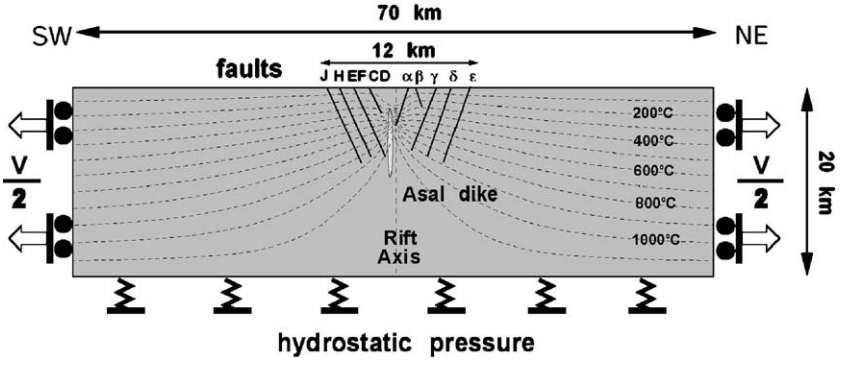

Fig. 6. Geometry and boundary conditions of the model. The section is submitted to 11 mm/year horizontal spreading. The model is loaded with gravitational body forces ($g = 9.81$ m/s^2). The hydrostatic foundation at the base of the model insures isostatic balance. The faults geometry is constrained from Ref. [15,27]. A simple static friction law is assumed on the faults. The thermal structure constrained from geothermal measurements and seismicity is initially imposed. A depth varying rheology (with strain rate and temperature) is assumed to account for elasto-brittle and ductile deformation. The long term (~100 ka) deformation is first calculated with no faulting and then by letting the faults slip freely. We impose the co-rifting slip on the faults EF, CD, α, β and γ and dilatation of the Asal dyke obtained from inversion of geodetic data [12,13,15]. The post-rifting phase is next computed by locking the faults and imposing a dyke inflation.

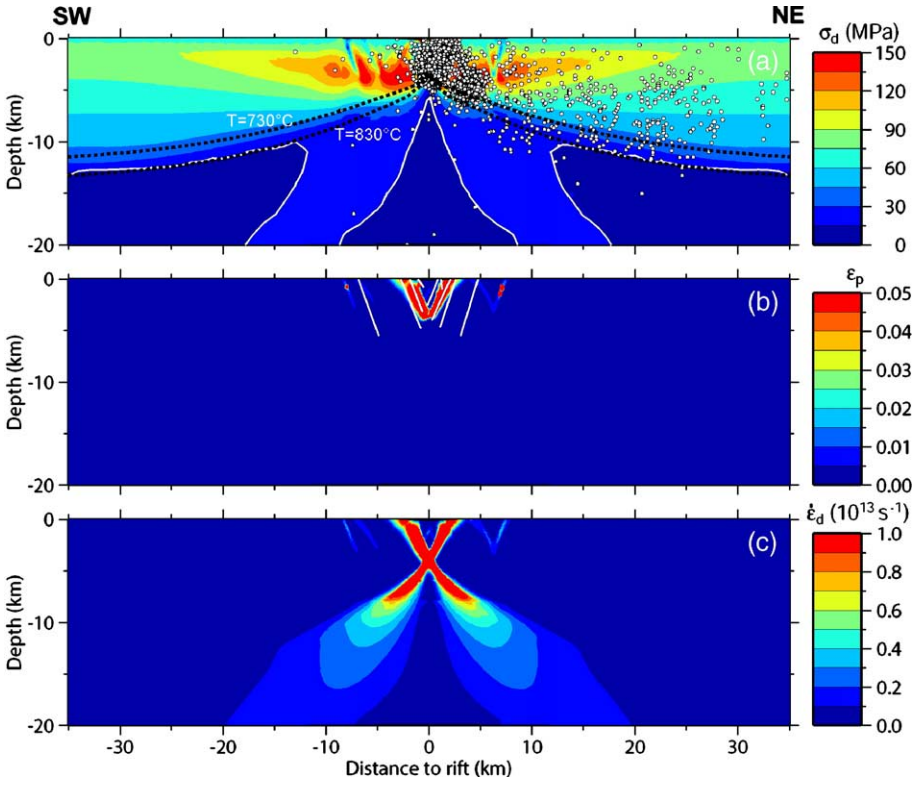

Fig. 7. Long-term (100 ka) state of stress (a) Deviatoric stress (shaded colour) and micro-seismicity since 1979 (white circles) along the cross section [25,30]. Black dotted lines give the depth of the 730–830 °C isotherm associated with the thickness of the seismogenic layer. (b) Plastic deformation (shaded colour) and faults' geometry inferred from geological observations and co-rifting data (white lines). (c) Deviatoric strain rate (shaded colour) showing a localized deformation area at depth.

Intense seismicity correlates with high second invariant of the deviatoric stress tensor,

$$\sigma_d = \sqrt{3\left[\sigma'^2_{xy} + \frac{1}{2}\left(\sigma'^2_{xx} + \sigma'^2_{yy}\right)\right]}, \quad (5)$$

where x and y are the horizontal and vertical component, respectively. We use the deviatoric stress rather than temperature field because the stress field depends both on temperature and on strain rate (see Eq. (3)). The increase of the seismogenic thickness with the distance to rift axis until 12–13 km is mainly associated with the depth of the 730–830 °C isotherm. This temperature is consistent with the 700–800 °C obtained from oceanic intraplate seismicity and transform fault earthquakes in the North Atlantic [42,43]. Fig. 7c shows the calculated second invariant of deviatoric strain rate tensor

$$\dot{\varepsilon}_d = \sqrt{3\left[\dot{\varepsilon}'^2_{xy} + \frac{1}{2}\left(\dot{\varepsilon}'^2_{xx} + \dot{\varepsilon}'^2_{yy}\right)\right]}. \quad (6)$$

The deep seismicity within 10 km of rift axis is explained by the high strain rate due to the ductile shear zone above the Asal–Ghoubbet rift.

The location and the dip angle of the inner rift fault are in remarkably good agreement with the calculated plastic strain ε_p (Fig. 7b). However this simple computation cannot explain the distribution of the slip rate estimated from topographic data: the cumulative plastic strain suggests that EF and γ are the most active faults over the last 100 ka when observations give the highest slip rate for the faults closest to the rift axis. This disagreement could be due to oversimplification of this approach. It is also possible that inflation of the shallow magma reservoir under the rift axis causes a local stress change, large enough to increase the slip of faults α and A.

4.2. Effect of magma injection

Next we introduced explicitly the active faults of the Asal–Ghoubbet rift, using the same initial and boundary conditions than in the previous modelling. The faults EF, CD, α, β and γ are constrained from co-rifting data [9,13,15], For the others active faults (J, H, δ and ε), inactive during the 1978 event, we use field observations [27] to constrain the location of faults'

upper edges and we assume a steep geometry at depth (dip angle = 70°). We set a friction coefficient allowing free slip on faults.

The calculated profile of vertical velocities exhibits a narrow zone of high subsidence rate (~12 mm/year) within 2.5 km of the rift axis. This pattern is consistent with the results of our previous modelling with plastic shear zones replaced here by faults. However the calculated subsidence rate is overestimated compared to vertical velocity obtained from Fieale deformation and Lake Asal highstand (Fig. 3). This suggests that over the last 100 ka the crustal thinning due to tectonic forces is partly balanced by magmatic injection [10]. In reality magmatism may feed a number of dykes or sills. For the purpose of the modelling we consider a single opening crack mimicking a single dyke. To simulate the effect of lava infilling we apply under the rift axis at a depth z_{infill} a velocity with a fixed vertical component V_{infill}. The value of z_{infill} plays a role in determining the width of the subsidence zone. Assuming z_{infill} between 2 and 4 km depth, does not significantly affect the velocity profile.

The increase of V_{infill} yields a profile of subsidence that closely mimics the observation (Fig. 3). The subsidence rate of Fieale deformation and Lake Asal highstand data are better explained with an injection rate of 10 and 5 mm/year, respectively. The difference between the Quaternary and Holocene subsidence rate suggests that rifting is not steady state [15], but rather affected by high variation of magma injection. As previously proposed [10], the high rate of injection over the last 100 ka could explain the high spreading rate (17–29 mm/year) estimated from the restored topography of the Fieale relative to the present day opening velocity of 11 mm/year between Arabia and Somalia.

The increase of V_{infill} also perturbs the simple fault slip distribution described above. First the stress change leads to an increase in the slip on faults close to the rift axis. Second it extends the zone of high deformation, which is accommodated by slip on faults farther from the rift axis. This suggests that slip distribution is controlled by both tectonic and magma injection, although it is difficult to quantify the relative effect of those two mechanisms from long term observations only.

5. Rifting cycle deformation

5.1. From co-rifting to post-rifting

The co-rifting displacements have been previously modelled using dyke inflation and fault slip embedded in a linear elastic medium [9,13,15]. Using both the temperature field and the state of stress obtained over 100 ka as initial condition, we impose a dyke opening of 1.5 m and fault slip distribution inferred from these previous studies (EF: 0.45 m; CD: 0.35 m; α: 0.45 m; β: 0.1 m; γ: 0.3 m). The calculated co-rifting displacement is consistent with both trilateration and levelling data projected along the study profile (Fig. 8). Nevertheless due to the two dimensional limitation of the modelling the calculated displacement overestimates both opening and subsidence close to the rift axis. The co-rifting displacement induces localized stress change in the inner rift to a depth of 7–8 km (Fig. 9a). This stress field is rapidly modified by viscoelastic relaxation. After only 6 years co-rifting stress beneath the dyke inflation zone is mainly relaxed, inducing a stress increase in the elastic part of the lithosphere (Fig. 9b). This implies a widening of the deformation zone during post-rifting period. Based on geodetic data showing a post-rifting velocity change in 1984–1986 (Fig. 3), we now consider two stages of post-rifting deformation: (1) from 1978 to 1984–1986 and (2) from 1984–1986 to 2003.

5.2. Post-rifting deformation until 1984–1986

Following the approach developed for the post-rifting episode in the Krafla system (north Iceland), we

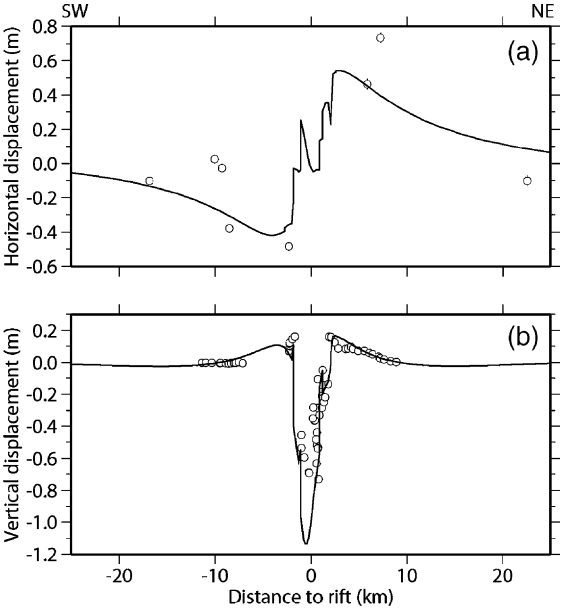

Fig. 8. Calculated (black line) and measured (circle) surface co-rifting displacements projected along the section shown in Fig. 1. The co-rifting faults model comes from [15] (a) Horizontal displacement. (b) Vertical displacement.

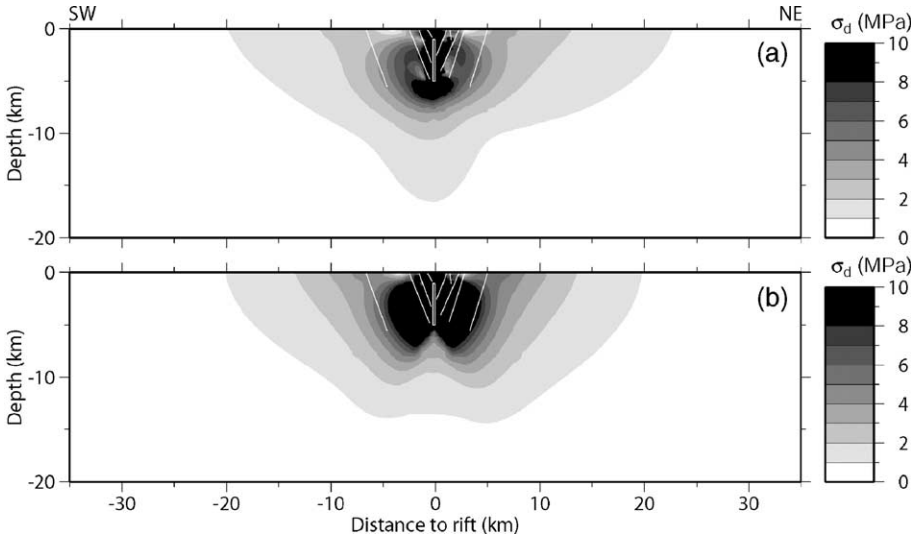

Fig. 9. Deviatoric stress change after the 1978 seismo-volcanic crisis. White lines indicate the location of both faults and dyke. (a) Co-rifting stress change. (b) Stress change after 6 years (1985).

begin with the effect of pressure change in a magma chamber on post-rifting deformation. We assume that the magma chamber can be approximated as a spherical chamber. Post-rifting horizontal velocities are given with respect to the centre of the magma chamber, close to the Ardukoba volcano (Fig. 10). We invert jointly horizontal and vertical velocity using the Mogi's equations [44]. Based on magnetotelluric study [32], we have fixed the radius of the magma chamber to 1 km. The best-fitting model is obtained for a depth of 6.2 km and a pressure change of 4.5 MPa (Fig. 10). The calculated velocities are inconsistent with the observations (RMS>5). This conclusion can be drawn directly from the lack of radial symmetric in the observed deformation. This suggests that (1) the geometry of the magma chamber is more complicated or (2) the post-rifting deformation is due to other processes, such as viscous relaxation, dike injection or fault creep. In the following we test the second hypothesis.

First, we favour viscoelastic behaviour for the lithosphere supported by the very high temperature gradients and the volcanism. We use the long term temperature field and the pre-stress due to both long-term and co-rifting as the initial condition. The post-rifting deformation is performed with a stretching rate of 11 mm/year. In the first years following the 1978 event, viscous relaxation is mainly controlled by viscosity of $0.5–1\times10^{18}$ Pa s near the rift axis. This value is consistent with the estimated viscosity of $\sim10^{18}$ Pa s obtained from geodetic measurements in the vicinity of the Krafla volcanic system in Iceland [21]. Viscous relaxation causes a zone of both uplift and opening within 6 km of rift axis (dotted line in Fig. 11). This pattern is in disagreement with post-rifting measurements. First the calculated opening rate of ~15 mm/year is inconsistent with trilateration measurements with at least a velocity stretching of 65 mm/year. Second the modelled narrow uplift zone within the inner rift cannot explain the measured large uplift beyond the rift shoulders. Thus it appears that the viscous relaxation is a minor part of the observed post-rifting deformation.

This result suggests that dyke inflation persisted for a few years after the crisis. To test this effect we use the same initial and boundary conditions except we apply a constant horizontal opening rate on both vertical faces of the dyke ranging from 0 to 20 cm/year. A dyke opening rate of 12 cm/year yields profile displacements that closely mimic both trilateration measurements and levelling data (Fig. 11). Due to infinite length of the dyke, the subsidence rate of the inner rift is overestimated by 10–15 mm/year, suggesting that a three-dimensional approach would have given a better fit.

The levelling data between 1979 and 1984–1985 gives asymmetric pattern of vertical velocity with a subsidence of the north-eastern part of the profile relative to the south-western one. As mentioned in the "data sets" section, this may be due to instrumental drift. Here we assume that this trend is real. Because the viscous relaxation of stress is mainly controlled by the temperature field, we propose that slightly offset of the dyke location with respect to the

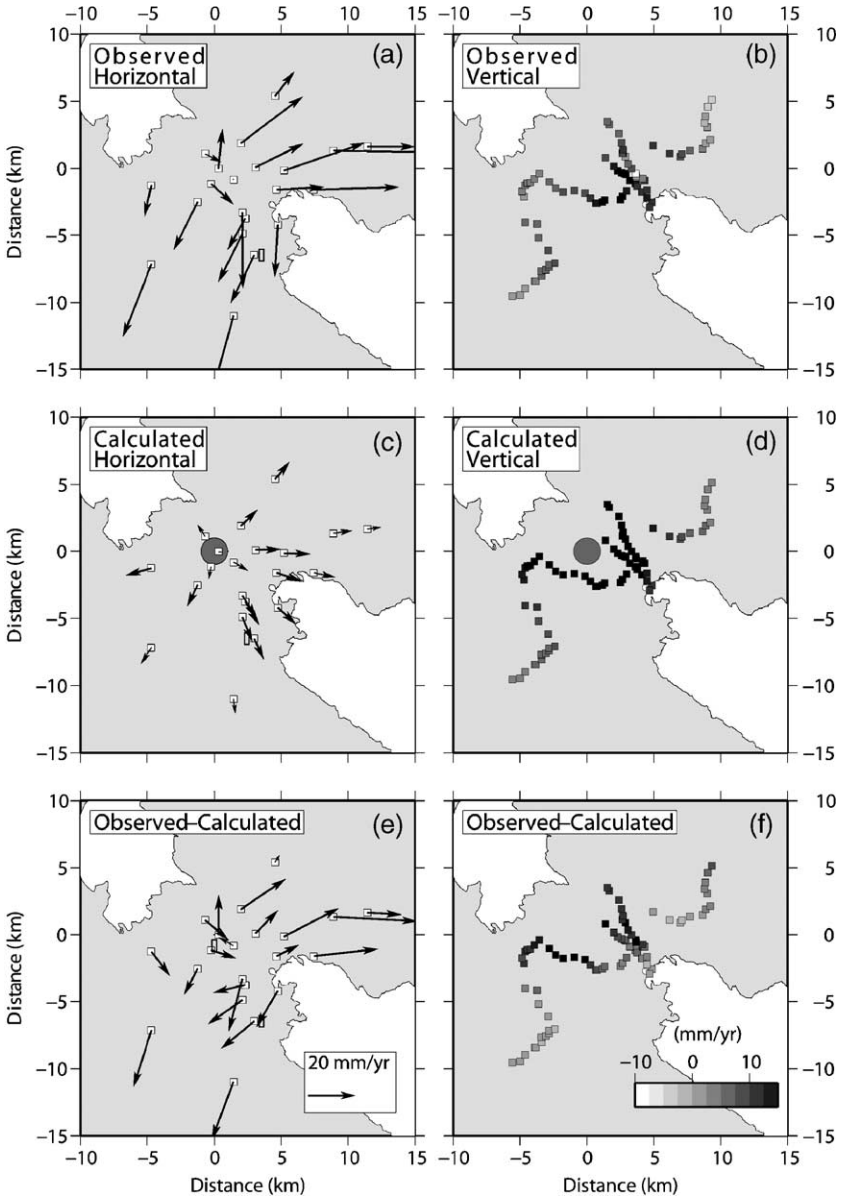

Fig. 10. Estimated pressure change in the magma chamber from Mogi's equation [44]. (a,b) Observed horizontal and vertical velocity between 1979–1984. (c,d) Calculated velocity from the best fitting model: pressure change of 4.5 MPa and depth of the magma chamber, 6.2 km. Grey circles give the location and the radius of the source of pressure. (e,f) Residual: observed–calculated velocity.

high temperature gradient of the rift axis could be the cause of this asymmetry. We move the dyke northward to a distance $x_{\text{dyke-axis}}$ between 0 and 100 m. We use a dyke opening rate of 12 cm/year. Due to the high lateral variation of temperature near the rift axis, our tests give the unexpected result that the horizontal velocities stay unchanged when the vertical velocities highly depends on $x_{\text{dyke-axis}}$. Fig. 12 shows that the pattern of levelling line leads to an offset of 15 m.

5.3. Post-and inter-rifting deformation since 1984–1986

The geodetic data indicates an abrupt opening rate decrease, from 65 to 17 mm/year, in the inner rift in 1984–1986 (Fig. 4g). This may reflect the end of the viscous relaxation of the co-rifting stress after 6–8 years. The non-linear rheology of the modelled lithosphere leads to post-rifting strain rate that cannot be simply matched from a simple exponential with a

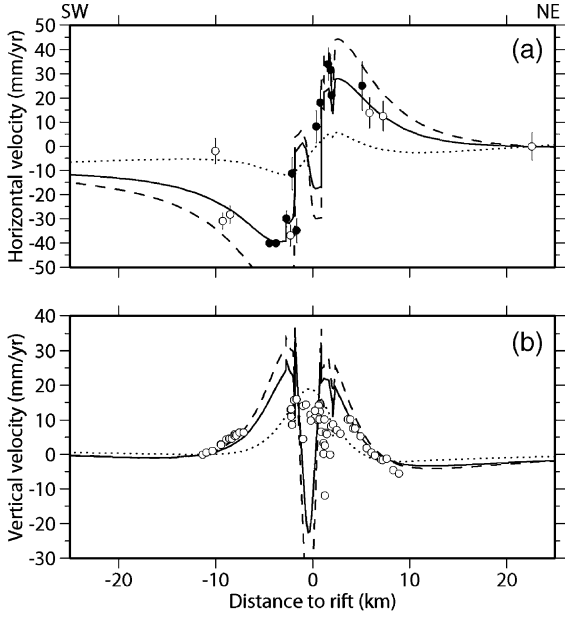

Fig. 11. Effect of dyke opening on post-rifting velocity. Dashed line, black line and dotted line give the calculated velocity for a dyke opening of 20, 12 and 0 cm/year, respectively. The dyke is located at 15 m south of the rift axis. (a) White and black circles give velocity from trilateration observations between 1979–1984 and 1979–1985, respectively [14]. Observed and calculated velocities are given with respect to the northernmost observed velocity. (b) Circles give measured vertical velocity from levelling observations during the 1979–1984 interval. Measured and calculated velocities are plotted with respect to the southernmost levelling benchmark.

constant relaxation time. In our modelling the lowest effective Maxwell viscosity of $0.5–1\times10^{18}$ Pa s below the rift axis gives a relaxation time of ~2–4 months. This suggests that the co-rifting stress close to the rift axis is fully relaxed after 6–8 years (see deviatoric stress change after 6 years on Fig. 9). However the decrease of viscous relaxation is a progressive process that cannot account for the abrupt feature of the velocity change. We therefore propose that the decrease in the opening rate in 1984–1986 is primarily controlled by the end of magma injection, at least in the dyke activated in 1978. Thus, to simulate the second-stage of post-rifting deformation, we use the same boundary conditions except on both vertical faces of the dyke, which are fixed 7 years after the seismo-volcanic crisis. This kinematic boundary condition generates at the upper and lower edge of the dyke an overpressure of P~20 MPa. Close the rift axis, the amplitude of average overpressure is comparable to co-rifting stress change. This suggests that pressure due to dyke inflation mainly controls the post-rifting stress after 6–8 years when the co-rifting stress change is fully relaxed.

The velocity obtained from this approach mimics qualitatively well the mean features of the observed profiles (Fig. 13) showing a higher opening rate in the inner rift relative to Arabia–Somalia motion and a wide uplift within 10 km of the rift axis. However the quantitative comparison between measured and calculated velocity reveals two major disagreements: first an asymmetric pattern of the observed horizontal velocity between the southern and northern flank of the rift and second a zone of subsidence of the inner rift. We interpret these disagreements as the effect of aseismic creep along the fault γ. We invert the velocity residual (observed-calculated) using the classical formulations for slip on a fault segment in a homogeneous elastic half space [45]. Fig. 13 shows that 13 mm/year of normal slip along the fault γ is required to fit both GPS between 1991 and 2003 and levelling data between 1984 and 2000. The depth of the lower and the upper edge of the creeping fault is 4 and 0.3 km, respectively. This is consistent with creep movement across the margin fault of the inner rift inferred from repeated levelling [14] and with recent seismological experiment showing clearly a zone of intense microseismic activity below the north-eastern shoulder of the rift.

In the foregoing we have assumed that the dyke inflation ends in 1985. We have tested the effect of this time t_{end} on the temporal variations in the opening

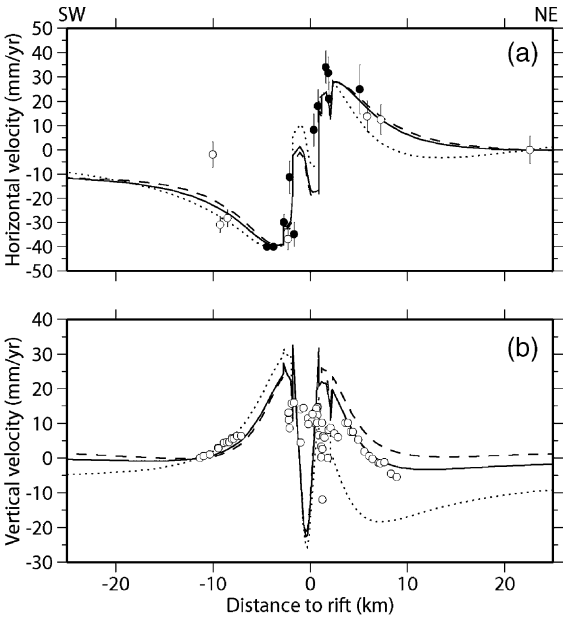

Fig. 12. Effect of rift axis location versus dyke position on post-rifting velocity. Dashed line, black line and dotted line give the calculated velocity for a dyke position of 0, −15 and −100 m, respectively. The imposed dyke opening is 12 cm/year. Symbols are the same as Fig. 9.

for the lines C–F, FG–CF and EP–DF (see points location on Fig. 1). Fig. 14 shows that the cumulative horizontal displacement is very sensitive to this parameter for t_{end} between 1984 and 1986. This clearly reveals that a constant and large dyke inflation of 12 cm/year until 1985 can explain the post-rifting data, although it is difficult to infer a unique temporal evolution of this rate from these observations. This requires a systematic study of the temporal evolution of the dyke opening, which is beyond the scope of this paper. The comparison between the geodetic data and our calculation suggests also that the deformation rate is constant since ~1990 and mainly controlled by tectonic forces including active fault creep and regional stretching.

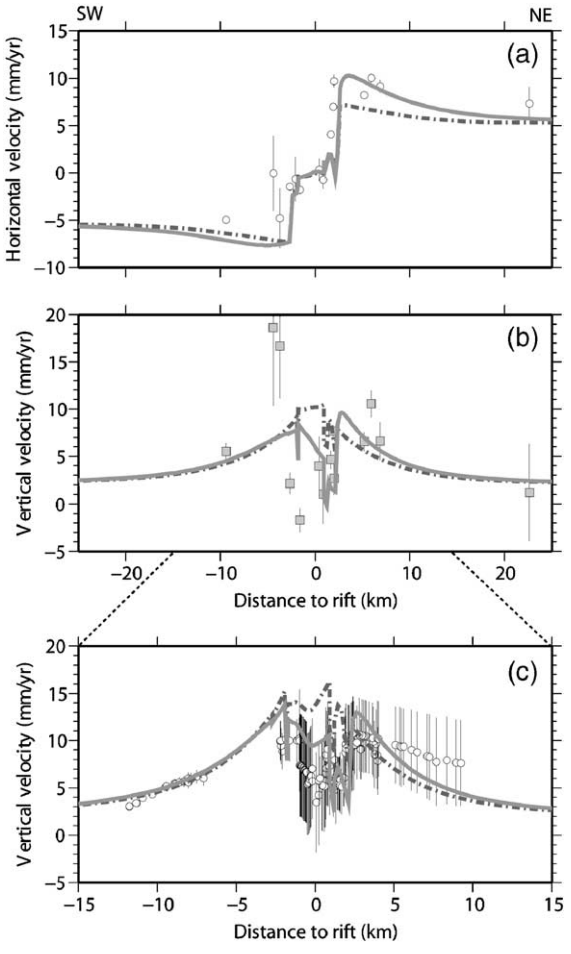

Fig. 13. Post- and inter-rifting displacement since 1985. Gray and dashed line indicate the calculated velocity with and without additional aseismic slip, respectively. This aseismic normal slip of 13 mm/year is imposed on the γ fault from 4 to 0.3 km depth. No dyke opening is imposed since 1985. (a) Horizontal GPS velocity from 1991 to 2003 [16] (circles). Error bars show the formal 1-sigma uncertainty of each measurement. (b) Vertical GPS velocity from 1991 to 2003 with respect to Somalian plate [16] (gray square). (c) Levelling measurements during the 1984–2000 interval with respect to the southernmost GPS data of the Fig. 11b (circles). Velocities uncertainties increase northward due the levelling line measurement only in one way (forward run).

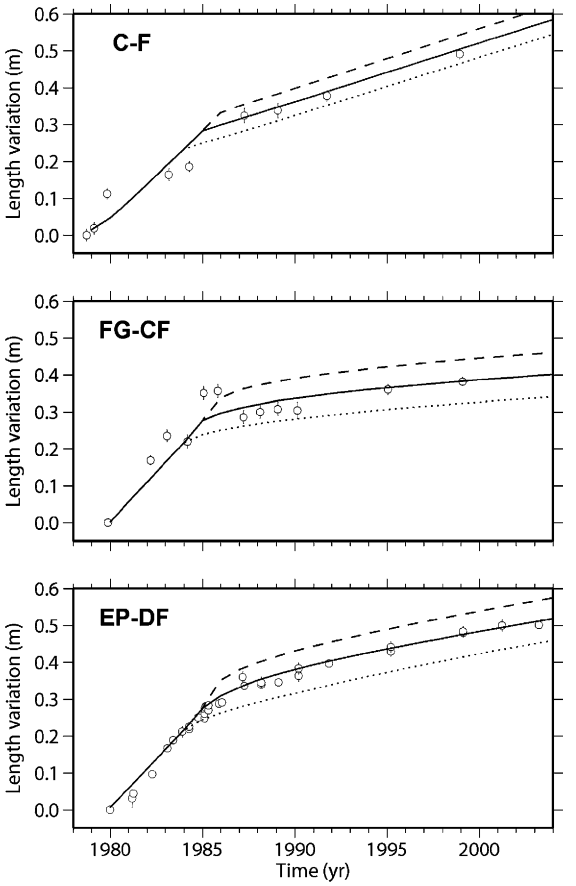

Fig. 14. Calculated and measured (circles) line length variation between 1979 and 2003 along the three profiles C–F, FG–CF and EP–DF. The line length variations are relative to the first measurements. Dotted line, black line and dashed line indicate the calculated length variation for no opening dyke since 1984, 1985 and 1986, respectively.

6. Conclusions

A two-dimensional model of deformation in the Asal–Ghoubbet rift has been derived from the analysis of geological observations, geophysical data and geodetic measurements. Our modelling is clearly limited by the two-dimensional approach. However it provides a way to study the relationship between data of deformation and structure over different time-scales. Our modelling demonstrates the internal consistency of the data sets and its compatibility with current understanding of the mechanics of crustal stretching. The results show the relative effect of regional stretching, viscous relaxation, magma intrusion and fault creep in the rifting

process in Asal, although all these mechanisms are clearly related to each other [46]: regional stretching inducing high temperatures, which favours both magma intrusion and fault creep.

According to our modelling, the active fault location and geometry is mainly controlled by thermal structure and magma intrusion within the crust. The thermal structure constrained from thermal wells and micro-seismicity explains most of the localization of the deformation in the inner rift. Magma injection is also required to explain the high slip rate on the faults close to the rift axis.

The comparison between calculated velocity and subsidence rate estimated from Fieale topography and Lake Asal Highstand suggests that rifting is not steady state, but rather controlled by high variation of magma injection. We find that over the last 9 ka the average injection rate is twice as slow as during the last 100 ka. The value of injection rate (5–10 mm/year) is about equal to the regional opening rate (11 mm/year) suggesting that volcanic processes play a major role in the long-term deformation in the Asal–Ghoubbet rift.

As previously suspected [47], our modelling of post-rifting deformation shown by trilateration measurements, levelling line and GPS data reveals a complex post-rifting mechanism. The very high temperature gradients, the distribution of micro-seismicity and volcanism may favor viscous relaxation for post-rifting deformation. However it appears that viscous relaxation is a minor part of the observed post-rifting deformation when compared to inferred post-rifting dyke opening. Our modelling suggests that a constant and large dyke inflation of 12 cm/year ending in 1985 is required to explain both the abrupt velocity change in 1984–1986 and the high opening rate within 10 km of rift axis as shown by trilateration data. Finally our modelling suggests that the asymmetric pattern of horizontal velocity since 1985 can be explained by creep on the γ fault.

Acknowledgments

This work was supported by the French program ACI Catastrophes Naturelles. We are grateful to many people who contributed to the field work since 1973. We greatly appreciated the discussions with Arnaud Mignan, Kurt Feigl, Isabelle Manighetti and Thora Arnadottir. The manuscript benefits from discussions with C. Ebinger and M. Casey. We thank Rebecca Bendick and Freysteinn Sigmundsson for constructive reviews, which greatly improve the manuscript. We thank Rebecca Bendick and Freysteinn Sigmundsson for constructive reviews, which greatly improve the manuscript. We thank Jean Chéry for providing the finite element code *ADELI*. All the figures were made with the GMT software (Wessel and Smith, 1991).

References

[1] V. Courtillot, A. Galdénao, J.L. Le Mouël, Propagation of an accreting plate boundary: a discussion of new aeromagnetic data in the Gulf of Tadjurah and southern Afar, Earth Planet. Sci. Lett. 47 (1980) 144–160.

[2] V. Courtillot, J. Achache, F. Landre, N. Bonhommet, R. Montigny, G. Féraud, Episodic spreading and rift propagation: new paleomagnetic and geochronologic data from the Afar nascent passive margin, J. Geophys. Res. 89 (1984) 3315–3333.

[3] L. Audin, I. Manighetti, P. Tapponnier, F. Métivier, E. Jacques, P. Huchon, Fault propagation and climatic control of sedimentation on the Ghoubbet Rift Floor: insights from the Tajouaraden cruise in the western Gulf of Aden, Geophys. J. Int. 144 (2001) 391–413.

[4] H. Hébert, C. Deplus, P. Huchon, K. Khanbari, L. Audin, Lithospheric structure of a nascent spreading ridge inferred from gravity data: the western Gulf of Aden, J. Geophys. Res. 106 (2001) 26345–26363.

[5] E. Wolfenden, C. Ebinger, G. Yirgu, A. Deino, D. Ayalew, Evolution of the northern Main Ethiopian rift: birth of a triple junction, Earth Planet. Sci. Lett. 224 (2004) 213–228.

[6] P. Tapponnier, J. Varet, La zone de Mak'aeassou en Afar: un equivalent emerge des 'failles transformantes' océaniques, C. R. Acad. Sci. Paris 278 (1974) 209–212.

[7] R. Hofstetter, M. Beyth, The Afar depression: interpretation of the 1960–2000 earthquakes, Geophys. J. Int. 155 (2003) 715–732.

[8] A. Abdallah, V. Courtillot, M. Kasser, A.Y. Le Dain, J.C. Lépine, B. Robineau, J.C. Ruegg, P. Tapponnier, A. Tarantola, Relevance of Afar seismicity and volcanism to the mechanics of accreting plate boundaries, Nature 282 (1979) 17–23.

[9] A. Tarantola, J.-C. Ruegg, J.C. Lépine, Geodetic evidence for rifting in Afar: a brittle-elastic model of the behaviour of the lithosphere, Earth Planet. Sci. Lett. 45 (1979) 435–444.

[10] J.B. de Chabalier, J.P. Avouac, Kinematics of the Asal Rift (Djibouti) determined from deformation of Fieale Volcano, Sciences 265 (1994) 1677–1681.

[11] F. Gasse, J.C. Fontes, Paleoenvironments and paleohydrology of a tropical closed lake (Lake Asal, Djibouti) since 10,000 yr B. P., Paleogeogr. Paleoclimatol. Paleoecol. 69 (1989) 67–102.

[12] J.C. Ruegg, F. Gasse, P. Briole, Mouvements du sol holocènes dans le rift d'Asal à Djibouti, C. R. Acad. Sci. Paris 310 (1990) 1687–1694.

[13] A. Tarantola, J.-C. Ruegg, J.C. Lépine, Geodetic evidence for rifting in Afar: 2. Vertical displacements, Earth Planet. Sci. Lett. 48 (1980) 363–370.

[14] J.C. Ruegg, M. Kasser, Deformation across the Asal–Ghobbet rift, Djibouti, Uplift and crustal extension, 1979–1986, Geophys. Res. Lett. 14 (1987) 745–748.

[15] R.S. Stein, P. Briole, J.C. Ruegg, P. Tapponnier, F. Gasse, Contemporary, Holocene, and Quaternary deformation of the Asal rift, Djibouti: implications for the mechanics of slow spreading ridge, J. Geophys. Res. 96 (1991) 21789–21806.

[16] C. Vigny, J.B. de Chabalier, J.C. Ruegg, P. Huchon, K. Feigl, R. Cattin, L. Asfaw, K. Kanbari, 25 years of geodetic measure-

ments along the Tadjoura-Asal rift system, Djibouti, East Africa, Submitted to J. Geophys. Res.
[17] A. Björnssonn, K. Saemundsson, P. Einarsson, E. Tryggvason, K. Grönvold, Current rifting episode in north Iceland, Nature 266 (1977) 318–323.
[18] A. Björnssonn, G. Johnsen, S. Sigurdsson, G. Thorbersson, E. Tryggvason, Rifting of the plate boundary in north Iceland 1975–1978, J. Geophys. Res. 84 (1979) 3029–3038.
[19] G.R. Foulger, C.H. Jahn, G. Seeber, P. Einarsson, B.R. Julian, K. Heki, Post-rifting stress relaxation at the divergent plate boundary in Northeast Iceland, Nature 358 (1992) 488–490.
[20] M.A. Hofton, G.R. Foulger, Postrifting anelastic deformation around the spreading plate boundary, north Iceland: 1. Modeling of the 1987–1992 deformation field using a viscoelastic Earth structure, J. Geophys. Res. 101 (1996) 25403–25421.
[21] M.A. Hofton, G.R. Foulger, Postrifting anelastic deformation around the spreading plate boundary, north Iceland: 2. Implications of the model derived from the 1987–1992 deformation field, J. Geophys. Res. 101 (1996) 25423–25436.
[22] F. Sigmundsson, H. Vadon, D. Massonet, Readjustment of the Krafla spreading segment to crustal rifting measured by satellite radar interferometry, Geophys. Res. Lett. 24 (1997) 1843–1846.
[23] T. Arnadottir, F. Sigmundsson, P.T. Delaney, Sources of crustal deformation associated with the Krafla, Iceland, eruption of September 1984, Geophys. Res. Lett. 25 (1998) 1043–1046.
[24] O. Henriot, T. Villemin, F. Jouanne, Long period interferograms reveal 1992–1998 steady rate reformation of Krafla volcano (North Iceland), Geophys. Res. Lett. 28 (2001) 1067–1070.
[25] J.C Lépine, A. Hirn, Seismotectonics in the Republic of Djibouti linking the Afar depression and the gulf of Aden, Tectonophysics 209 (1992) 65–86.
[26] I. Manighetti, Dynamique des systèmes extensifs en Afar, PhD thesis IPGP Paris, 6 (1993).
[27] I. Manighetti, P. Tapponnier, P.Y. Gillot, V. Courtillot, R. Armijo, J.C. Ruegg, G. King, Propagation of rifting along the Arabia–Somalia plate boundary: into Afar, J. Geophys. Res. 103 (1998) 4947–4974.
[28] L. Zan, G. Gianelli, P. Passerini, C. Troisi, A. Omar Haga, Geothermal exploration in the Republic of Djibouti: thermal and geological data of the Hanlè and Asal areas, Geothermics 19 (1990) 561–582.
[29] BRGM, Construction d'un modéle synthétique du champ géothermique d'Asal, Rapport du BRGM 82 (1982) SGN 951 GTH.
[30] C. Doubre, Structure et mécanismes des segments de rift volcano-tectoniques; etudes de rifts anciens (Ecosse et Isalande) et d'un rift actif (Asal–Ghoubbet), PhD Thesis Université du Maine 420 pp (2004).
[31] J.C. Ruegg, Structure profonde de la croûte et du manteau supérieur du Sud-Est de l'Afar d'après les données sismiques, Ann. Geophys. 31 (1975) 329–360.
[32] Pham Van Noc, D. Boyer, J.L. Le Mouël, V. Courtillot, Identification of a magma chamber in the Ghoubbet–Asal rift (Djibouti) from a magnetotelluric experiment, Earth Planet. Sci. Lett. 52 (1981) 372–380.
[33] V. Ballu, M. Diament, P. Briole, J.C. Ruegg, 1985–1999 gravity field variations across the Asal Rift: insights on vertical movements and mass transfer, Earth Planet. Sci. Lett. 208 (2003) 41–49.
[34] F. D'Amore, D. Giusti, A. Abdallah, Geochemistry of the high-salinity geothermal field of Asal, Republic of Djibouti, Africa, Geothermics 27 (1998) 197–210.
[35] M. Mlynarski, J. Zlotnicki, Fluid circulation in the active emerged Asal rift (east Africa, Djibouti) inferred from self-potential and Telluric–Telluric prospecting, Tectonophysics 339 (2001) 455–472.
[36] R. Hassani, D. Jongmans, J. Chéry, Study of plate deformation and stress in subduction processes using two-dimensional numerical models, J. Geophys. Res. 102 (1997) 17951–17965.
[37] N.L. Carter, M.C. Tsenn, Flow properties of continental lithosphere, Tectonophysics 136 (1987) 27–63.
[38] S.H. Kirby, A.K. Kronenberg, Rheology of the lithosphere: selected topics, Rev. Geophys. 25 (1987) 1219–1244.
[39] M.C. Tsenn, N.L. Carter, Upper limits of power law creep of rocks, Tectonophysics 136 (1987) 1–26.
[40] A.B. Watts, Isostasy and Flexure of the Lithosphere, Cambridge University Press, 2001.
[41] M. Jean, G. Touzot, Implementation of unilateral contact and dry friction in computer codes dealing with large deformations problems, Mec. Theor. Appl. 7 (1988) 145–160.
[42] D.A. Wiens, S. Stein, Age dependence of oceanic intraplate seismicity and implication for lithospheric evolution, J. Geophys. Res. 88 (1983) 6455–6468.
[43] E.A Bergman, S.C. Solomon, Transform fault earthquakes in the North Atlantic: source mechanisms and depth faulting, J. Geophys. Res. 93 (1988) 9027–9057.
[44] K. Mogi, Relations between the eruptions of various volcanoes and the deformations of the ground surfaces around them, Bull. Earthq. Res. Inst. 36 (1958) 99–134.
[45] S.J. Singh, S. Rani, Crustal deformation associated with two-dimensional thrust faulting, J. Phys. Earth 41 (1993) 87–101.
[46] A.M. Rubin, D.D. Pollard, Dike-induced faulting in rift zones of Iceland and Afar, Geology 16 (1988) 413–417.
[47] J.C. Ruegg, M. Kasser, J.C. Lépine, Strain accumulation across the Asal–Ghoubbet rift, Djibouti, East Africa, J. Geophys. Res. 89 (1984) 6237–6246.